

Design and fabrication of prototype piezoelectric adjustable X-ray mirrors

JULIAN WALKER,^{1,*} TIANNING LIU,^{1,2} MOHIT TENDULKAR,² DAVID N. BURROWS,³ CASEY T. DEROO,⁴ RYAN ALLURED,⁴ EDWARD N. HERTZ,⁴ VINCENZO COTRONEO,⁴ PAUL B. REID,⁴ ERIC D. SCHWARTZ,⁴ THOMAS N. JACKSON,^{1,2} AND SUSAN TROLIER-MCKINSTRY¹

¹Materials Science and Engineering Department and Materials Research Institute, Millennium Science Complex, Pennsylvania State University, University Park, PA, 16802, USA

²Center for Thin Film Devices, Department of Electrical Engineering, Pennsylvania State University, University Park, PA, 16802, USA

³Department of Astronomy and Astrophysics, Pennsylvania State University, University Park, PA, 16802, USA

⁴Harvard-Smithsonian Center for Astrophysics, 60 Garden Street, Cambridge, MA, 02138, USA

*Julian.walker@ntmu.no

Abstract: Lynx, a next generation X-ray observatory concept currently under study, requires lightweight, high spatial resolution X-ray mirrors. Here we detail the development and fabrication of one of the candidate technologies for Lynx, piezoelectric adjustable X-ray optics. These X-ray mirrors are thin glass shell mirrors with Cr/Ir X-ray reflective coatings on the mirror side and piezoelectric thin film actuators on the actuator side. Magnetron sputtering was used to deposit metal electrodes and metal-oxide piezoelectric layers. The piezoelectric ($\text{Pb}_{0.995}(\text{Zr}_{0.52}\text{Ti}_{0.48})_{0.99}\text{Nb}_{0.01}\text{O}_3$) was divided into 112 independent piezoelectric actuators, with 100% yield achieved. We discuss the fabrication procedure, residual thermal stresses and tuning of the Cr/Ir coating stress for the purposes of stress balancing.

© 2018 Optical Society of America under the terms of the [OSA Open Access Publishing Agreement](#)

1. Introduction

Lynx is a NASA mission concept under study for consideration in the 2020 Astrophysics Decadal Survey. Lynx operates in the X-ray regime (0.1 – 10 keV) and will observe supermassive black holes at high redshifts, map the process of galactic evolution and trace stellar activity. The Lynx observatory will feature a telescope assembly with a comparable angular resolution to the Chandra X-ray Observatory, with a 0.5 arcsecond half power diameter (HPD) point spread function (PSF) on axis, a 1 arcsecond HPD over a large field of view (10 arc minutes by 10 arcminutes), and a 30 times greater effective area (2 m²) at 1 keV [1,2]. Such an assembly is made possible by thin, low mass-per-collection-area X-ray optics, and will consist of nested grazing incidence mirrors. One technology being developed to achieve the necessary high angular resolution of the Lynx telescope is piezoelectric adjustable X-ray optic(s) (PAXO) [3,4]. PAXO are thin shell mirrors which can have the optical figure of the mirror corrected post manufacture to achieve high (< 0.5 arcsecond HPD PSF) angular resolution. The piezoelectric adjustment is required to improve the mirror figure achieved by high temperature slumping of thin glass sheets [4]. Piezoelectric adjusters would also be applicable to silicon or full-shell glass optics. In all cases, the dynamic figure adjustment capability of PAXO enables adjustment of the mirror figures after mounting or even after launch (i.e. on-orbit correction). The fabrication of prototype PAXO mirrors is thus an important part of the development of high resolution optics for next generation X-ray observatories.

PAXO development in the past decade began with flat substrates. Initial studies determined a suitable commercially available glass for forming and compatibility with the

piezoelectric processing required for the PAXO application [5,6]. Later prototype development identified radio frequency (RF) magnetron sputtering as the preferred method of piezoelectric film deposition and refined the deposition and crystallization parameters to maximize yields [6,7]. The next series of flat mirror prototypes were used to perform initial influence function measurements during the activation of individual piezoelectric cells and test the use of thin film transistors with the PZT to enable row column addressing for voltage control of the piezoelectric cells on each mirror [8]. The present generation of PAXO mirrors demonstrated the successful transition from flat to curved mirrors and provided proof-of-concept relative figure correction to a targeted optical surface figure with an accuracy of 1.2 arcseconds HPD [9,10]. While this first generation of curved mirrors did not implement thin film transistors and did not achieve absolute optical figure correction, important developments necessary for the advancement of PAXO technology were demonstrated.

The current generation of PAXO are 101.6 mm × 101.6 mm thin glass shells (0.4 mm thick), which have an array of piezoelectric actuators on the actuator side (convex) and a reflective mirror coating on the mirror side (concave) (Fig. 1) [9,10]. The figure adjustability results from the converse piezoelectric effect, where an applied electric field produces an in-plane strain in the piezoelectric actuator, resulting in precise changes to the mirror Fig [11]. $\text{Pb}_{0.995}(\text{Zr}_{0.52}\text{Ti}_{0.48})_{0.99}\text{Nb}_{0.01}\text{O}_3$ (PZT)-based piezoelectric materials are already widely utilized for nanoscale positioning systems [12] and piezoelectric micromechanical systems (piezoMEMS) [13,14]. Thus, PZT-based compositions are excellent candidate materials for achieving high precision adjustment of X-ray optics. However, the fabrication of PAXO presents many challenges. Crystallization of PZT layers requires thermal excursions of up to 650°C, and the mirror needs to survive the heat treatment without introducing distortions to the mirror figure that are too large for correction by the actuators [9,10]. Minimizing figure distortion during processing requires uniform temperatures during heating and balancing of the integrated stresses (stress × thickness, MPa·μm) of the layers deposited on the actuator and mirror sides of the PAXO. The piezoelectric actuators also need to exhibit a high (near 100%) yield of the individual actuators to enable full correctability of the mirrors [3,7,9,10]. Achieving high actuator yields requires rigorous substrate cleaning, control of the PbO content of films during synthesis, and greater than 80 μm resolution of top electrode features that are lithographically patterned on the curved mirrors.

Here, the current prototype PAXO design and fabrication is presented. Details of the actuator processing, the resulting electrical properties of the piezoelectric actuators and piezoelectric displacements achieved are reported. These mirrors were used to demonstrate measured figure corrections to virtual optical surface of 10–15 arcseconds HPD, resulting in simulated corrected mirrors with performance 1–3 arcseconds HPD, as well as investigate the influence functions of the optical surface during actuation of the piezoelectric cells [10]. The stress developed during processing is investigated and identifies key methods for reducing stress and improving uniformity in future mirrors. The introduction of the stress balancing method also provides a method for producing future PAXO prototypes with correctable figures.

2. Design and fabrication of piezoelectric actuators

The PAXO prototype consisted of a total of six thin film layers, four on the actuator side of the mirror and two on the reflective side of the mirror (Figs. 1(a) and 1(b)). The actuator side of the mirror was processed before deposition of the X-ray reflective coating (Cr/Ir) on the reflective side of the mirror. This sequence of processing was followed in order to prevent damage of the X-ray reflective coating after deposition, and to preserve the as-deposited stress state of the Cr/Ir coating by avoiding exposing it to the temperature excursions required for crystallization of the piezoelectric layer.

Curved *Corning Eagle XG* glass substrates 0.4 mm thick were an approximation of the Wolter I geometry utilized for grazing incidence X-ray reflection. The radius of curvature

(ROC) of the slumped glass was 220 mm which is near the minimum radius required for the Lynx optical design featuring PAXO (150 mm). The curvature of the glass was achieved by slumping, where a flat glass piece 200 mm \times 200 mm was placed on a commercially manufactured mandrel with a magnetron sputtered Pt release layer, and heated to $\sim 745^\circ\text{C}$ for 24 hours in a box furnace [5]. The curved glass pieces were laser cut to 101.6 \times 101.6 mm (4 \times 4 inch) dimensions.

Prior to film deposition the glass pieces were cleaned using a five-step process [9]. (1) Substrates were washed with a commercial solution *KleanAR* (*Avantor Perf Mat-Macron Lab*) containing sulphuric and chromic acid. Glass was placed in the solution and ultrasonicated at 45°C for 5 minutes. The glass was then removed from the *KleanAR* and rinsed in flowing deionized (DI) water for 3 minutes. (2) The glass was submerged in acetone and the container was returned to the ultrasonic bath for 5 minutes. (3) The glass was transferred from acetone to isopropanol and returned to the ultrasonic bath for a further 5 minutes without being allowed to dry. (4) The glass was removed from the isopropanol and rinsed in flowing DI water for 3 minutes before being placed in container with DI water and returned to the ultrasonic bath for 5 minutes. (5) After removal from the DI water, the glass was blown dry using compressed nitrogen gas. As a final part of the cleaning process, the glass pieces were treated to remove any residual organic contamination in an *M4L RF Gas Plasma system* (*PVA, TePla*) for 2 minutes with 200 W radio frequency (RF) power, 150 sm^3/sec oxygen, 50 sm^3/sec helium and a 550 mTorr regulated chamber pressure to remove any residual organic contamination.

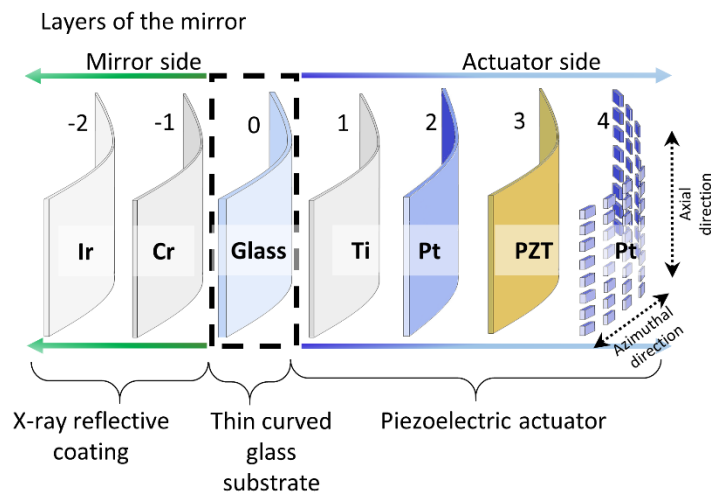


Fig. 1. A schematic of the piezoelectric adjustable optic mirror separated into the individual layers. Each layer is labelled according to the material. The glass substrate is denoted as zero, the layers on the actuator side (convex side) increase from 1 to 4 in the order in which they are deposited, and the layers on the mirror side are given decreasing (negative) integers, -1 and -2.

The first layer of the actuator was a $0.02\ \mu\text{m}$ thick coating of Ti (layer 1 in Fig. 1), which was included as an adhesion layer due to its ability to readily oxidize and thus form a strong bond with both the glass surface and the Pt layer. Scanning electron microscopy (SEM) images of the Ti film were taken using a *Leo 1530 field emission scanning electron microscope* (FESEM). As shown in Fig. 2a, the SEM images exhibit nanometer microstructural features. A $0.1\ \mu\text{m}$ layer of Pt was then deposited without removing the mirror from the vacuum system (Layer 2 in Fig. 1). Both the Ti and Pt metal films were sputter deposited using a direct current (DC) magnetron system (*Kurt J. Lesker CMS-18*) at

room temperature ($\sim 18\text{--}22^\circ\text{C}$) and a pressure of 2 mTorr. The vertical distance between the magnetron and the substrate, referred to as the vertical throw distance, was 136 mm. The sputtering target was below the substrate in what is referred to as a bottom up configuration. The substrate was positioned with the central axis of the cylindrical sputter chamber intersecting its center, perpendicular to the axial and azimuthal substrate axes. The 76.2 mm (3 inch) diameter target was offset by 82.5 mm (3.25 inches) from the central axis of the chamber and was angled at 15° towards the center. A power density of 4.4 W/cm^2 for deposition produced growth rates of approximately 1.0 \AA/s and 2.4 \AA/s for the Ti and Pt, respectively. The Pt layer acted as the bottom electrode and buffer layer between the piezoelectric and the glass, and had nanometer scale microstructural features (Fig. 2b), and predominantly (111) orientation observed from the 111 Pt peak labeled in the XRD pattern in Fig. 2c. The (111) orientation and fine microstructural features of the Pt observed here are suitable for the subsequent deposition and crystallization of high quality PZT films. Significant changes to the Pt microstructure can indicate reduced density or increased roughness, which may in turn degrade the quality of the PZT deposited on top.

The piezoelectric PZT layer (layer 3 in Fig. 1) was deposited on top of the Pt in three layers with crystallization occurring after each layer. Growing the films in multiple steps like this was critical for maintaining high yield and low electrical loss, as it minimized the chance that defects in a single layer could percolate through the entire film [7]. The PZT coatings were radio frequency (RF) magnetron sputtered in a *Kurt J. Lesker CMS-18* vacuum sputter tool. The target composition was $\text{Pb}_{0.995}(\text{Zr}_{0.52}\text{Ti}_{0.48})_{0.99}\text{Nb}_{0.01}\text{O}_3$ with 5 atomic % excess PbO . The chamber configuration was the same as that detailed for the Ti and Pt deposition. However, a different chamber was used in order to prevent contamination between the metal and metal oxide materials. An argon chamber pressure of 4 mTorr and an RF power density of 2.0 W/cm^2 were used. Crystallization was carried out after each layer was deposited using a temperature of 650°C for 1 minute in a rapid thermal annealing (RTA) furnace.

The PZT composition was chosen due to its high piezoelectric coefficients (i.e. $d_{33}\approx 200\text{ pC/N}$, $d_{33,f}\approx 90\text{ pC/N}$ and $e_{31,f}\approx -10\text{ C/m}^2$) and wide application among piezoMEMS and microelectronic actuator devices [12–15]. The resulting PZT films had the perovskite structure with no preferred crystallographic orientation and no detectable secondary phases Fig. 2(c). The microstructure had an average grain size of 375 nm, determined by the line intercept method (ASTM E 112), with no porosity visible from the surface Fig. 2(d). Atomic force microscopy (AFM) was conducted with an *Asylum Research* tool in contact tapping mode to determine the PZT surface roughness. The root mean squared (RMS) surface roughness of the PZT was 4.6 nm with a peak to valley roughness of 29 nm Fig. 2(e). This surface roughness plays no part in the reflection of X-rays but is important to monitor in order to gauge the uniformity and reproducibility of the PZT films. PZT surface roughness can assist with adhesion of the Pt top electrode layers. The microstructural features and phase purity (single phase) of the PZT film have an important influence of the piezoelectric properties and reliability of the piezoelectric material. The microstructure of PZT films is strongly dependent on the deposition method used and is a useful indicator of film uniformity and quality.

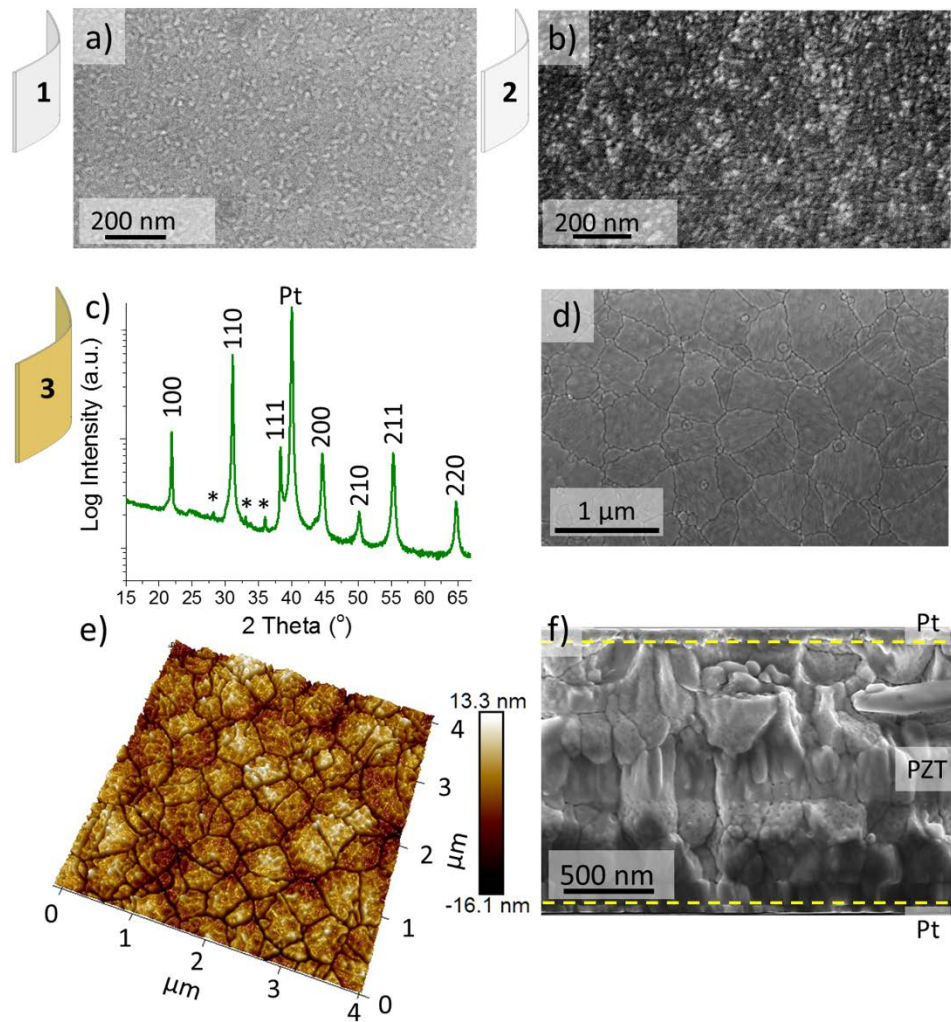


Fig. 2. a) Surface SEM micrograph of an as-deposited layer 1, the 0.02 μm thick Ti adhesion layer. b) Surface SEM micrograph of an as-deposited layer 2, the 0.10 μm thick Pt bottom electrode layer 0.10 μm thick. c) XRD pattern of 3 layer 1.5 μm thick crystallized PZT. PZT peaks are labeled by their pseudo-cubic Mindices and the single platinum peak is labelled. Asterisks indicate peaks from other X-ray wavelengths. d) surface SEM of PZT layer microstructure. e) AFM topography image of a 4 x 4 μm region of the PZT surface. f) SEM of a cross section of the Pt/PZT/Pt actuator.

The PZT films were approximately 1.6 μm thick with blocky microstructure Fig. 2(f). Nanometer-sized pores were unevenly distributed throughout the film, with regions with more pores correlating approximately with the upper half of each 0.5 μm separately-crystallized layer. As a result, the porosity is likely related to the loss of PbO from the surface of the films due to volatilization during crystallization [7]. While porosity is detrimental to the dielectric and piezoelectric properties of a PZT film [16,17], the concentration of pores was low enough that the films were able to achieve the desired dielectric and piezoelectric responses [3,7].

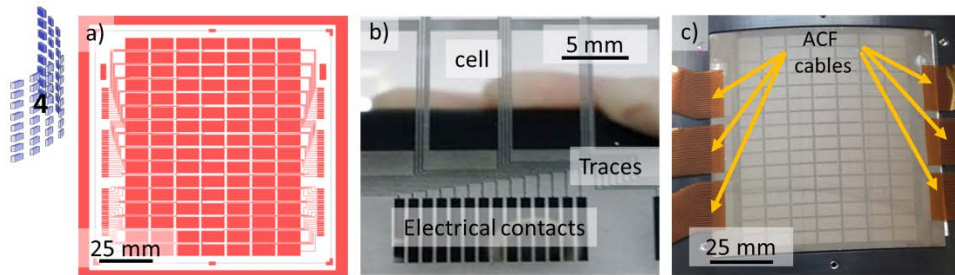


Fig. 3. Pt top electrode layer patterned by photolithography. a) An image of the full electrode pattern design for prototype mirrors. b) A magnified optical image of Pt deposited on a clear curved glass substrate patterned for the top electrode piezoelectric cell array. The three key components of the pattern are labeled, piezoelectric cell, traces and electrical contacts. c) A photograph of the finished PAXO mirror prototype with bonded ACF cables.

A critical component of the current PAXO prototype design was the division of the PZT film into individual piezoelectric cells, each one independently controllable. The mirror design consisted of a matrix of seven rows and sixteen columns for a total of 112 piezoelectric cells, each with dimensions of $5\text{ mm} \times 10\text{ mm}$ and 1 mm spacing between cells Fig. 3(a) [9,10]. Slope errors in the axial dimension have a greater impact on the imaging performance of a grazing incidence mirror relative to slope error in the azimuthal dimension by a factor of $1/\sin(\theta)$, where θ is the grazing angle incident on the mirror. Thus, the smaller cell dimension in the axial direction was designed to allow a greater degree of spatial control of the mirror figure parallel to incoming X-rays. The effectiveness of this piezoelectric cell configuration was previously explored using finite element modeling [18].

The piezoelectric cell division was achieved by patterning of the Pt top electrodes using a double layer photolithography process (Layer 4 in Fig. 1). For full details refer to Walker et al. [9]. Polydimethylglutarimide-based *LORIA* (*Micro-Chem Corp., Newton, MA*) was used for the first photoresist layer and *SPR3012* (*Micro-Chem Corp., Newton, MA*) for the second layer. Each layer was spin coated using a carrier wafer which held the curved glass pieces in place during spinning by four points of contact, one on each mirror edge. A flexible mask was used to expose the photoresist with UV for 10 seconds in the desired pattern and was followed by developing in commercial resist developer *MF-CD26* (*Dow Chemical Co., Midland, MI*). The $0.1\text{ }\mu\text{m}$ thick Pt top electrodes were deposited at room temperature and Ar pressure of 5 mTorr using the same deposition method as for the bottom electrode. Three groups of $1\text{ mm} \times 5\text{ mm}$ electrical contacts for the piezoelectric cells were positioned parallel to the axial edges of the mirror on both sides. Electrical traces $100\text{ }\mu\text{m}$ wide connected the piezoelectric cells to the electrical contacts Fig. 3(b).

Anisotropic conductive films (ACF) bonding was used to connect thin flexible cables to the mirror. ACF bonding is a commercially established approach for making electrical connections to liquid crystal display panels and other electronic packages [19-21]. Custom ACF electrical cables were made with Cu traces spaced equidistant to the electrical contacts patterned at the mirror's axial edge Fig. 3(c). Each Cu trace was connected to the electrical contacts by using a bonding tool able to apply temperature and pressure with high precision. First, the ACF tape was tacked to the mirror surface using a temperature of 90°C and pressure of 1 MPa for 15 seconds applied through the tip of the bonder. Then the bond was cured at a temperature of 180°C and a pressure of 1 MPa. The connected Cu traces were then linked to an electrical channel junction box for voltage control of each piezoelectric cells [10,22]. Future generations of PAXO prototypes will also have a layer of thin film transistors on top of the Pt top electrodes that will provide row-column addressing to reduce the number of electrical connections required to control the voltage to each cell [8].

3. Residual thermal stress of the actuator side of the mirror

The prototype mirror was found to have a non-uniform figure distortion that was too large to be corrected by the piezoelectric actuators and as a result was only suitable for demonstration of relative figure correction [10]. Subsequent investigation revealed that the source of the figure distortion was non-uniform stress of the actuator side of the mirror, caused by a temperature gradient ($\Delta T > 80^\circ\text{C}$) experienced during crystallization using the RTA.

To further study the development of residual thermal stress resulting from actuator fabrication, test samples were fabricated on flat 0.4 mm thick Corning Eagle XG glass substrates approximately 100 mm \times 100 mm. The stress associated with each layer and each step of the fabrication process was determined. Flat samples were used so that a *Tencor p16* + contact profilometer could be used to determine the change in curvature of the substrate after each process step. Samples were placed on a wafer mount to provide repeatable sample alignment. The mount consisted of three equidistant pins on which the sample is placed and three alignment pins which enable a repeatable x and y position of the sample. A contact weight of 2 mg and tip speed of 2000 $\mu\text{m}/\text{sec}$ was used over an 80 mm measurement length. A total of six measurements were made per wafer, with each measurement offset by rotating the wafer 60° clockwise. The average change in curvature of each measurement was determined and the Stoney equation (Eq. (1)) was used to estimate the film stress by assuming isotropic mechanical properties, uniform film and substrate thickness, and that the substrate thickness greatly exceeded the film thickness [23,24]. The six measurements were used to determine a two dimensional stress profile of the wafers and an average stress.

$$\sigma_f = \frac{E_s h_s^2}{h_f 6(1 - \nu_s) \kappa}, \quad (1)$$

where σ_f is the stress of the deposited film, E_s is the Young's modulus of the substrate, h_s is the thickness of the substrate, κ is the change in the radius of curvature, h_f is the thickness of the film and ν_s is the Poisson's ratio of the substrate. For PAXO, both the thickness and stress of each layer is important for the stress balancing process and thus, the results are discussed in terms of integrated stress (stress \times thickness, $\text{MPa}\cdot\mu\text{m}$).

The curvature of the flat glass substrates was measured initially after cleaning, and again after each process step. For this study, two samples were prepared by depositing 10 nm of Ti and 50 nm of Pt as the bottom electrode. For the two samples shown in Fig. 4(b), the change in the curvature after bottom electrode deposition suggested similar integrated stresses of -40 $\text{MPa}\cdot\mu\text{m}$ to -45 $\text{MPa}\cdot\mu\text{m}$ (the negative value indicates compressive stress). The difference in stress of these films deposited with identical sputter parameters is associated alignment error and starting substrate deviation from a uniform radius of curvature. For thin films (e.g. tens of nm) or low stress films this error can be significant as the change of curvature is small relative to the initial curvature of the substrate.

Two different thermal profiles were used during crystallization of the PZT samples on flat substrates Fig. 4(a). The low temperature crystallization profile ($T_{\text{max}} = 550^\circ\text{C}$) had a ramp rate of $10^\circ\text{C}/\text{min}$ and hold temperature of 18 hours; the high temperature crystallization profile ($T_{\text{max}} = 650^\circ\text{C}$) utilized a ramp rate of $20^\circ\text{C}/\text{min}$ and a hold time of 2 minutes. Both processes were completed in the same box furnace. Residual thermal stresses were considered a major contributor to the stress of the actuator of the PAXO mirrors and the use of the two profiles allowed for the assessment of the impact of crystallization temperature. PZT films prepared by each profile were found to have comparable microstructures and electrical properties, so from the point of view of the PZT actuator functionality, both profiles were suitable.

Next, 0.5 μm of PZT was deposited by RF sputtering; both layers exhibited integrated stresses of -30 $\text{MPa}\cdot\mu\text{m}$ (Fig. 4(b)). The integrated stress of the films changed significantly on

crystallization of the PZT layer, flipping from compressive to tensile with a value of 65 MPa· μm for the low temperature crystallized film and 80 MPa· μm for the high temperature crystallized film. Both the Ti/Pt and PZT layers contributed to the integrated stress estimated after the first crystallization step, as both experienced the elevated temperature for the first time [25–27]. The thermal excursion associated with crystallization induces residual thermal stress resulting from the mismatch of thermal expansion coefficients of the film and the substrate (Eq. (2)). Thus, the higher integrated stress of the high temperature crystallization (650°C) was expected.

$$\sigma_{Therm} = E_f (\alpha_f - \alpha_s) \frac{\Delta T}{(1 - \nu_f)}, \quad (2)$$

where E_f is the Young's modulus of the film, α_f and α_s are the thermal expansion coefficients of the film and the substrate respectively, ΔT is the difference between the maximum and minimum temperatures experienced and ν_f is the Poisson's ratio of the film.

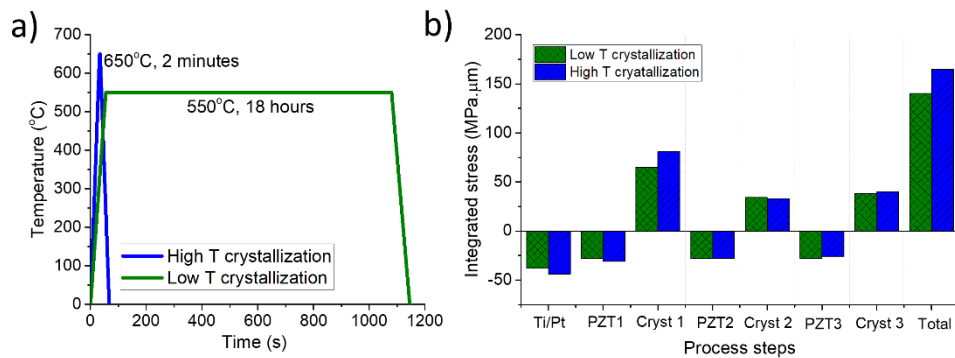


Fig. 4. a) Temperature-time profiles for the two heating schedules used to crystallize PZT during the stress study. b) Integrated stress after each processing step of a PAXO mirror for samples crystallized by the two temperature-time profiles. The total stress was determined from the final change in the ROC of the sample after the third crystallization. The numbers denote the deposition layer and the temperature cycle.

The second 0.5 μm thick PZT layer had an integrated stress of -28 MPa· μm after deposition for both samples. Upon crystallization, the stress of the PZT layers again changed from compressive to tensile, 35 MPa· μm and 80 MPa· μm for low and high temperature crystallization, respectively. Repetition of this measurement process for the third PZT layer again yielded compressive integrated stresses for the “as deposited” PZT films of -30 MPa· μm and -25 MPa· μm , with tensile integrated stresses after crystallization of 40 MPa· μm for both low and high temperature crystallizations respectively. As the Ti/Pt layer is subject to the temperature excursion during the first crystallization step, it was assumed that no change in stress of the Ti/Pt occurred during the crystallization steps for the second and third PZT layers. As a result, the integrated stress measured after crystallization of the second and third PZT layers was assumed to represent the residual thermal stress of the PZT layer being crystallized.

The integrated stress for the whole actuator side of the mirror after the final crystallization varied from 140 MPa· μm to 165 MPa· μm for the low and high temperature crystallizations profiles, respectively Fig. 4(b). This indicates that a lower crystallization temperature can be used to reduce the residual thermal stress of the actuator side of the mirrors. However, when the Ti/Pt layer was assumed not to contribute to the integrated stress (i.e. the measurements of PZT layers two and three) no trend was observed that linked the increased crystallization

temperature to an increase in the integrated stress of the PZT. Thus, we attribute the main difference in the residual thermal stress between the two processes to the temperature's impact on the Ti/Pt layers, not the PZT.

The similar thermal residual stresses experienced at 550°C and 650°C for the PZT can be explained by changes in the domain state induced as the film is cooled through the Curie transition temperature (T_c) at 350°C [28–30]. Upon cooling PZT through the T_c , the crystal structure transitions from a paraelectric phase with cubic symmetry (i.e. lattice parameters a , b and c are equal) to a ferroelectric phase with a non-cubic symmetry (e.g. a tetragonal symmetry, where lattice parameters $a = b \neq c$). The ferroelectric phase develops nanometer scale regions with different crystallographic orientations, called domains. As the phase transition is associated with a volume change and the ferroelectric structure that ensues has nonequivalent lattice parameters, preferential orientation of ferroelectric domains at T_c can relax thermal stresses [28–30]. The similar residual thermal stresses observed for the crystallized PZT films are therefore likely the result of the structural transition at T_c and the resulting ferroelectric domain orientation of each film.

The measured integrated stresses indicate that the Ti/Pt bottom electrode has a significant influence on the total integrated residual thermal stress of the actuator side of the mirrors, despite making up < 15% of the total thickness. Therefore, two methods for reducing the total integrated stress of the actuators of PAXO prototypes are to reduce the PZT crystallization temperature to 550°C, and to reduce the thickness of the Ti/Pt layer from 0.1 μm to 0.05 μm .

4. Balancing actuator stress with the stress of the reflective coating

Effective stress balancing of PAXO prototypes is required to counteract the mirror figure distortion that results from the piezoelectric actuator processing; this can be achieved by matching the integrated stress of the Cr and Ir coating on the reflective side of the mirror to the integrated stress of the actuator side of the mirror. This approach to stress balancing involved two key steps: (1) manipulating the deposition of Ir to target a maximum film stress, and (2) increasing the thickness to target the integrated stress value of the actuator side of the mirror. The Cr and Ir layers (labeled -1 and -2 in Fig. 1) were deposited by room temperature DC sputtering with the same *Kurt J. Lesker CMS-18* system and magnetron-substrate configuration used for the Ti and Pt depositions. The pressure for Cr deposition was 5 mTorr while for Ir the pressure was varied over the range 7.5 to 20 mTorr. The test Cr and Ir coatings for stress analysis were deposited on 500 μm thick Si wafers with a 100 nm thick SiO_2 thermal oxide layer (*Nova*) [31]. Stress balancing was later successfully performed on a curved PAXO mirror prototype.

As Cr readily oxidizes, it was used only as an adhesion layer and Ir was used to control the integrated stress. To match the integrated stress of the actuator side of the mirror both the stress and the thickness of the Ir were regulated. The stress of the Ir film could be controlled by adjusting the Ar pressure in the vacuum chamber during deposition [32–36], and the thickness could be increased by increased sputtering time. Changing the chamber pressure impacted the mean free path of Ir ions in the plasma, and thus influenced the energy of the Ir ions bombarding the substrate. The stress of the deposited films resulted from a combination of the film's elastic modulus and molar volume, and the energetics of the deposition.

To achieve the first step of the stress balancing process, a stress-pressure profile for DC sputtered Ir films was determined and the pressure required for maximum tensile stress identified Fig. 5(a). The Ir stress was investigated as a function of Ar chamber pressure while all other sputter parameters were kept constant. A transition from compressive to tensile stress occurred abruptly between 7.5 and 10 mTorr with stresses changing from -1500 MPa to 750 MPa and an approximately zero stress occurring at a pressure of 8.8 MPa. This transition was consistent with the trends reported by Thornton et al. [33–35]. The transition from tensile to compressive stress is generally explained by the onset of ion-peening at lower pressures and the competition between energetic particle bombardment and oblique deposition, which

change the microstructure and induce the transition to compressive stress. Above 10 mTorr, the tensile stress slowly relaxed towards zero with increasing chamber pressure; films deposited at 20 mTorr had stresses of 100 MPa. The pressure of 11 mTorr was chosen as a stable condition to deposit Ir films with near maximum stress.

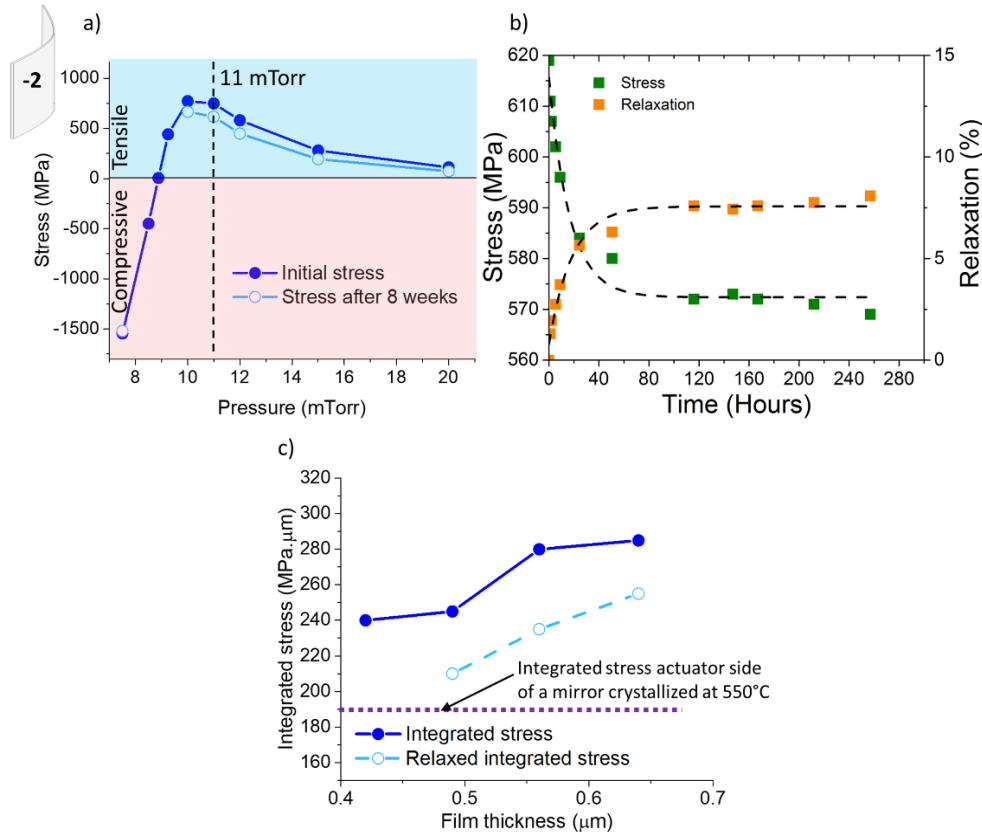


Fig. 5. a) Stress as a function of Ar chamber pressure during deposition of 100 nm Ir films at room temperature, measured immediately after deposition and eight weeks after deposition. b) The stress and percentage of stress relaxation of a 100 nm thick Ir film deposited at 11 mTorr with stress measured periodically as a function of time. The black dashed lines are exponential function fits to the data added as a guide to the eye. c) Integrated stress as a function of total thickness for 20 nm Cr films deposited at 7.5 mTorr plus Ir films deposited at 11 mTorr where the Ir thickness was varied to increase the total integrated stress. Integrated stress data were measured immediately after deposition and the relaxed integrated stress was measured eight weeks after deposition.

Interestingly, after a period of eight weeks the magnitude of the stress in each film decreased by as much as 15% Fig. 5(a). No micro-cracking was observed in the films, and thus the change in stress was attributed to some other mechanism of stress relaxation. In thin polycrystalline metal films, inelastic deformation mechanisms such as dislocation plasticity within grains and diffusional flow of matter between grain boundaries and the free surface have been proposed [36]. At room temperature, however, it is expected that there is insufficient energy for diffusional mass flow, and thus the relaxation observed in Ir films was thought to be related to dislocation glide, as observed for Cu films [37]. Oxidation of Ir at room temperature was also considered a possible cause of stress relaxation in the Ir coatings; however, the high oxidation resistance of Ir is well known [38]. For this reason, oxidation was not considered a likely cause of stress change in the Ir films. Adsorption of moisture at pores could also contribute to the observed room temperature stress relaxation of Ir films.

A subsequent study of a film's stress as a function of time was conducted on a 100 nm thick Ir film deposited at 11 mTorr and the stress was measured periodically over a ten-day period Fig. 5(b). The stress was observed to relax exponentially as a function of time, reducing by a total of 8% in ten days, with approximately 75% of the stress reduction occurring in the first 24 hours. In order to confirm the stress relaxation behavior over a wider sample range, twenty different Cr/Ir coatings with varying Cr/Ir thickness ratios and total thicknesses of 0.10-0.6 μm were measured and re-measured multiple times over a time frame of up to eight weeks after the initial measurement. In all cases a stress relaxation of 7-15% was observed, leading to the conclusion that the stress relaxation stabilized within 2 to 8 weeks of deposition. It may be possible to reduce the relaxation by adjusting the deposition conditions to develop higher initial densities, or by coating the films to prevent moisture ingress.

Test mirror coatings with 20 nm of Cr and Ir deposited at 11 mTorr with varied thicknesses were deposited with integrated stresses spanning the range of values expected to be required based on the actuator layer investigation. These coatings were measured immediately after deposition and again eight weeks later in order to gauge the initial and relaxed integrated stress Fig. 5(c). The integrated stress increased with Ir thickness as expected, and spanned a wide integrated stress range even after the films were observed to relax by 8-15% of the initial stress value. These films were proof of concept that the stress balancing approach could be applied to PAXO mirrors.

Next the stress balancing approach was applied to a PAXO mirror prototype. An integrated stress of 190 $\text{MPa}\cdot\mu\text{m}$ was measured for a prototype PAXO mirror crystallized in a box furnace at 550°C. This stress is indicated by the dashed line in Fig. 5(c). For the measurement a *Nanovea* optical profilometer was used. The stress balancing approach was used to deposit a Cr/Ir coating on to the reflective side of the mirror achieving a value of 170 $\text{MPa}\cdot\mu\text{m}$, within approximately 10% of the target integrated stress. We note that for this stress balancing attempt, the stress relaxation was not factored into the Ir thickness calculation, and therefore the error between the target integrated stress and the achieved integrated stress of the Cr/Ir coating may be further decreased by including extra thickness to compensate for the stress relaxation. It is also worth noting that the integrated stress of 190 $\text{MPa}\cdot\mu\text{m}$ for the PAXO prototype was higher than that observed for the actuator stress of flat glass test pieces (140 $\text{MPa}\cdot\mu\text{m}$); the likely reason for this is the reduced thickness of the Pt bottom electrode (50 nm instead of 100 nm) used for the flat glass study. Future PAXO prototypes will adopt the 50 nm Pt layer thickness.

As PAXO technology continues to be developed, modified approaches for stress balancing and mirror coatings are needed. While the current approach detailed here satisfies the requirement of balancing stress, the surface roughness of the Ir is inadequate for high efficiency X-ray reflectance. AFM measurements of Cr/Ir coatings with sufficient integrated stress to match the PZT actuator side of the mirror indicated that coating roughness was in the range of 3.4 to 5.2 nm RMS, depending on the thickness, with thicker coatings having a higher roughness. While X-ray test measurements have not yet been conducted on these Cr/Ir films, it is known that their roughness is up to an order of magnitude higher than the current achievable roughness of X-ray reflective Ir coatings [39] or the roughness anticipated for the Lynx mirrors. However, it is important to note that thus far in this work no attempt has been made to reduce the Ir film roughness, and this is a key focus of future work. While the current Cr/Ir films are suitable for studying function of the piezoelectric actuators they are not suitable as telescope grade coatings. The increase in Ir roughness with increasing thickness highlights the need to reduce the actuator stress by using lower crystallization temperature and keeping layer thicknesses as thin as possible.

Additional approaches for stress balancing are presently under investigation. Post actuator processing by precision polishing of the reflective side of the mirror to adjust stress has recently been established as a potential technique. Efforts in this area have achieved mirror

figure changes on the correct order of magnitude but without the desired spatial resolution. Additional techniques such as deposition of high-stress-low-roughness layers such as SiO_2 beneath the Cr/Ir may be suitable approaches. Meanwhile, the work of Broadway et al., where 0.5 nm RMS Ir coatings were achieved by RF magnetron sputtering under varied Ar pressure conditions serves as a useful benchmark for sputter deposited X-ray coatings [39].

5. Actuator functionality and optical surface adjustment

Following fabrication, the relative permittivity and dielectric loss was measured for 112 cells of a PAXO prototype mirror. Dielectric permittivity and loss tangent measurements were made with a *Hewlett Packard 4284A Precision LCR Meter* using an AC frequency of 1kHz and amplitude of 30 mV. The PAXO prototype exhibited a piezoelectric yield of 100%, with full functionality of all 112 piezoelectric cells. The average relative permittivity 1270 ± 39 to 1 standard deviation (1σ) and the dielectric loss was 0.047 ± 0.011 (1σ). These values excluded one outlier, which, although exhibiting high loss (0.56), could be poled and exhibited full piezoelectric functionality. The dielectric measurements indicated that the yield and uniformity of the film was high, and were representative of high quality PZT films grown by sputter deposition with no preferred orientation [13,14]. Piezoelectric cells were subsequently poled at electric fields of 66 kV/cm ($10 V_{dc}$) before the displacement of the mirror during actuation of the piezoelectric cells investigated.

The out-of-plane deflection (i.e. perpendicular to the glass surface, referred to as z displacement) resulting from activation of each piezoelectric cell on a curved mirror was measured using Wavefront Sensor Metrology with an *Imagine Optics HASO128 Shack-Hartmann Wavefront Sensor*, incorporated into a double-pass wavefront measurement system with a 6 inch diameter telescope and a cylindrical computer-generated hologram (CGH) Fig. 6(a). The data have a pixel size of approximately 0.8 mm, were inpainted (digitally modified) to be free of metrology artifacts and interpolated onto a common grid. Before data for average displacement were collected, each piezoelectric cell was poled at $10 V_{dc}$ for 40 minutes. For the measurement the mirror was mounted using seven flexure supports and one fixed support, four supports spaced equidistant at each axial edge. Bonded flex cables were attached to zero insertion force connectors Fig. 6(b). Further details of the mount and experimental setup can be found in DeRoo et al. [10]. A typical spatial distribution map of the z displacement across the mirror, resulting from activation of a single piezoelectric cell by $10 V_{dc}$, is given in Fig. 6(a). A peak in z displacement occurred underneath the actuated piezoelectric cell, while the mirror experienced negative z displacements with minimum values towards the axial edges (i.e. left and right sides). Inset (i) shows the z displacement profile in the azimuthal direction in plane with the piezoelectric cell. Inset (ii) shows a similar profile for the axial direction of the mirror. A peak-to-valley (PV) z displacement of $1.24 \mu\text{m}$ was observed. The peak displacement was typical for that observed from all piezoelectric cells; however, precise influence functions observed varied depending on the location of the piezoelectric cell on the mirror.

The slumped glass mirror substrates, prior to actuator fabrication, typically achieve an optical performance of approximately 10 arcsecond HPD (single reflection at 1 keV) with an axial figure PV difference of $2.53 \mu\text{m}$ [10]. During application of $10 V_{dc}$ to a single piezoelectric cell, a positive z displacement of approximately $0.5 \mu\text{m}$ is observed directly under the piezoelectric cell with an axial width of 5 mm, indicating that an approximate gradient of figure change induced is on the order of 10 arcseconds, while the as slumped mirrors have a performance on the order of 10 arcseconds HPD. This indicates that, in principle, the typical slope error in the slumped glass figure should be correctable by piezoelectric actuators.

Despite the hypothetical correction that could be provided by the piezoelectric actuators, analysis of the current generation of PAXO mirrors revealed that the piezoelectric fabrication induced significant distortion of the mirror figure due to large temperature gradients during

crystallization, resulting in an axial figure PV difference of $31.9 \mu\text{m}$ [10]. This non-uniform distortion could not be effectively mitigated by the stress balancing approach outlined in Section 4, due to the non-uniformity, and thus the mirror figure was distorted beyond the correctable limits. However, DeRoo et al. were able to perform a proof of concept of the piezoelectric figure correction by performing relative corrections to virtual optical surfaces [10]. This process involved using spatially filtered distortion maps with a Legendre polynomial fit to the distortion data and keeping contributions only up to the 10th order. Six different figure distortions were simulated and figure improvements of approximately $3.5 \times$ were achieved with final performances of 1 to 3 arcseconds HPD. The resulting distortions of the optical surface and full details of the simulated figure correction approach are reported by DeRoo et al. [10].

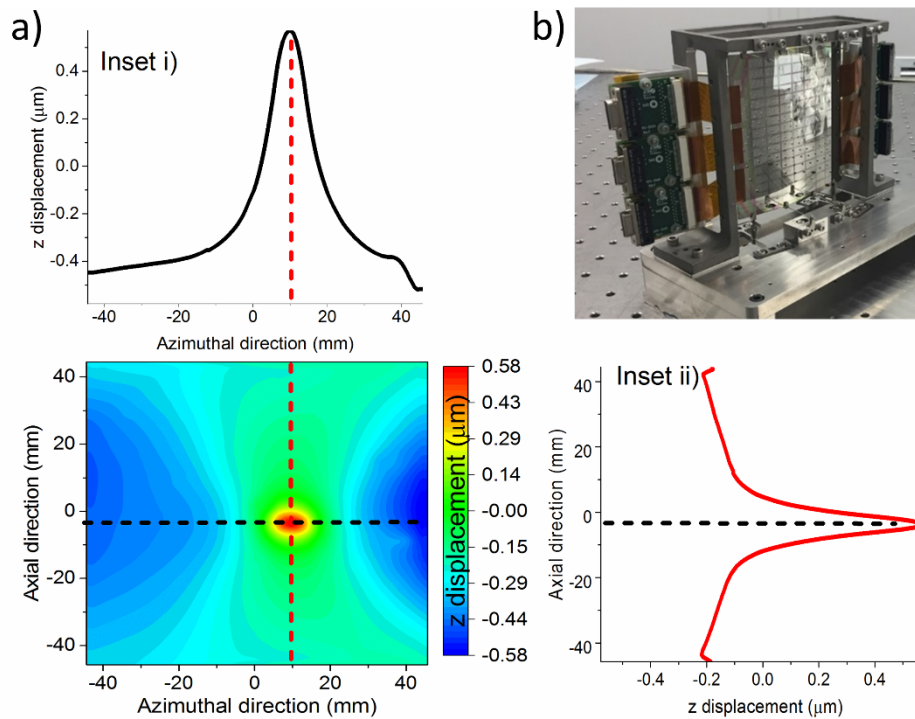


Fig. 6. a) Out-of-plane (z direction) displacement spatial distribution map of the PAXO mirror prototype measured by optical metrology during application of 10 V to a single poled piezoelectric cell. Inset (i) shows the z displacement in the azimuthal direction occurring in the plane represented by the horizontal (black) dashed line. Inset (ii) shows the z displacement in the axial direction in the plane represented by the vertical (red) dashed line. The displacement was normalized to the mirror figure at zero applied voltage. b) Photograph of the mounted prototype PAXO mirror used for assessing optical performance and out-of-plane displacement of the optical surface during actuation of piezoelectric actuators [10].

As a result of the non-uniform figure distortion of the current generation of PAXO mirrors absolute figure correction has not yet been demonstrated. However, the identification and removal of the temperature gradient causing the figure distortion, together with the reduced crystallization temperature, reduced Pt thickness and the stress balancing approach, the next generation of PAXO mirrors should have significantly improved figures post fabrication to facilitate absolute figure correction.

6. Conclusions

Here the fabrication and design of the current generation of PAXO prototype mirrors used to demonstrate relative figure correction of a cylindrically curved X-ray mirror with a ROC of 220 mm was detailed. The piezoelectric actuator processing achieved 100% yield of 112 piezoelectric cells that were lithographically patterned on the curved surface, exhibiting average relative permittivity and dielectric losses of 1270 and 0.047. These values are representative of high quality $\text{Pb}_{0.995}(\text{Zr}_{0.52}\text{Ti}_{0.48})_{0.99}\text{Nb}_{0.01}\text{O}_3$ films. A study of the integrated stress caused by actuator layer deposition and crystallization revealed that for crystallization temperatures of 550°C and 650°C, the total integrated stresses of the actuators were 140 MPa- μm and 165 MPa- μm respectively. By systematically studying the stress contributions of each layer of the actuator it was determined that the integrated stress of the PZT layers showed little dependence on the crystallization temperatures. Instead the Pt bottom electrode was found to be the cause of increased actuator stress with increased crystallization temperature. Therefore, reducing the crystallization temperature and reducing the thickness of the Pt layers was identified as a means of reducing the overall integrated stress of the actuator side of the mirror.

Reducing the integrated stress of the actuator layer is important because this stress is critical to the process of stress balancing. An approach of stress balancing the mirror by matching the integrated stress of the actuator side of the mirror with the integrated stress of the reflective Cr/Ir coating was developed. First, the Cr layer was kept thin, to act as an adhesion layer. Then a stress-deposition pressure study was conducted to find the maximum stress that could be achieved during room temperature magnetron deposition of Ir. This was approximately 700 MPa at 10 mTorr Ar pressure. Finally, the deposition pressure to 11 mTorr was used to deposit the stress balancing X-ray reflective coating. 11 mTorr was chosen to provide a buffer from tensile-compressive stress conversion region that occurred rapidly at pressures between 10 and 7 mTorr. The stress balancing approach was carried out on a curved mirror prototype achieving an actuator/mirror stress differences of 10%. These results indicate that in principle a stress balancing approach allow the production of future PAXO prototypes that can be corrected to sub-arcsecond HPD by the piezoelectric actuators.

Funding

National Aeronautics and Space Administration (NASA) (NASA 15-APRA15-0131, NNX16AG29G, NNX17AF66G).

References

1. J. A. Gaskin, R. Allured, S. R. Bandler, S. Basso, M. W. Bautz, M. F. Baysinger, M. P. Biskach, T. M. Boswell, P. D. Capizzo, K.-W. Chan, M. M. Civitani, L. M. Cohen, V. Cotroneo, J. M. Davis, C. T. DeRoo, M. J. DiPirro, A. Dominguez, L. L. Fabisinski, A. D. Falcone, E. Figueroa-Feliciano, J. C. Garcia, K. E. Gelmis, R. K. Heilmann, R. C. Hopkins, T. Jackson, K. Kilaru, R. P. Kraft, T. Liu, R. S. McClelland, R. L. McEntaffer, K. S. McCarley, J. A. Mulqueen, F. Özel, G. Pareschi, P. B. Reid, R. E. Riveros, M. A. Rodriguez, J. W. Rowe, T. T. Saha, M. L. Schattenburg, A. R. Schnell, D. A. Schwartz, P. M. Solly, R. M. Suggs, S. G. Sutherland, D. A. Swartz, S. Trolier-McKinstry, J. H. Tutt, A. Vikhlinin, J. Walker, W. Yoon, and W. W. Zhang, "Lynx Mission Concept Status," *Proc. SPIE* **10397**, 103970S (2017).
2. R. H. T. Wilke, R. L. Johnson-Wilke, V. Cotroneo, W. N. Davis, P. B. Reid, D. A. Schwartz, and S. Trolier-McKinstry, "Sputter deposition of PZT piezoelectric films on thin glass substrates for adjustable x-ray optics," *Appl. Opt.* **52**(14), 3412–3419 (2013).
3. D. A. Schwartz, R. Allured, J. A. Bookbinder, V. Cotroneo, W. R. Forman, M. D. Freeman, S. McMudroch, P. B. Reid, H. Tananbaum, A. A. Vikhlinin, R. L. Johnson-Wilke, S. E. Trolier-McKinstry, R. T. H. Wilke, T. N. Jackson, J. I. Ramirez, M. V. Gubarev, J. J. Kolodziejczak, S. L. O'Dell, and B. D. Ramsey, "Technology Requirements for a Square Meter, Arcsecond Resolution Telescope for X-Rays: The SMART-X Mission," *Proc. SPIE* **9208**, 920806 (2014).
4. V. Cotroneo, R. Allured, C. T. DeRoo, K. L. Gurski, V. Marquez, P. B. Reid, and E. D. Schwartz, "Thermal forming of glass substrates for adjustable optics," *Proc. SPIE* **10399**, 10399 (2017).
5. R. T. H. Wilke, R. L. Johnson-Wilke, V. Cotroneo, S. McMudroch, P. B. Reid, D. A. Schwartz, and S. Trolier-McKinstry, "Fabrication of adjustable cylindrical mirror segments for the smart-X telescope," *IEEE Trans. Ultrason. Ferroelectr. Freq. Control* **61**(8), 1386–1392 (2014).

6. R. L. Johnson-Wilke, R. T. H. Wilke, V. Cotroneo, W. N. Davis, P. B. Reid, D. A. Schwartz, and S. Trolrier-McKinstry, "Improving yield of PZT piezoelectric devices on glass substrates," *Proc. SPIE* **8503**, 85030A (2012).
7. M. Wallace, "Performance of PZT based MEMS devices with integrated ZnO Electronics," PhD doctoral dissertation, Pennsylvania State University, Department of Materials Science and Engineering (2016).
8. J. Walker, T. Liu, M. Tendulkar, D. Burrows, C. T. DeRoo, R. Allured, E. Hertz, V. Cotroneo, P. Reid, E. D. Schwartz, T. N. Jackson, and S. Trolrier-McKinstry, "Design and fabrication of adjustable x-ray optics using piezoelectric thin films," *Proc. SPIE* **10399**, 103991K (2017).
9. C. T. DeRoo, R. Allured, V. Cotroneo, E. N. Hertz, V. Marquez, P. B. Reid, E. D. Schwartz, A. A. Vikhlinin, S. Trolrier-McKinstry, J. Walker, T. N. Jackson, T. Liu, and M. Tendulkar, "Deterministic figure correction of piezoelectrically adjustable slumped glass optics," *J. Astron. Telesc. Instrum. Syst.* **4**(1), 019004 (2018).
10. N. N. Rogacheva, *The Theory of Piezoelectric Shells and Plates* (Taylor and Francis Group, 1994).
11. H. Liu, B. Lu, Y. Ding, Y. Tang, and D. Li, "A motor-piezo actuator for nano-scale positioning based on dual servo loop and nonlinearity compensation," *J. Micromech. Microeng.* **13**(2), 295–299 (2003).
12. P. Muralt, R. G. Polcawich, and S. Trolrier-McKinstry, "Piezoelectric thin films for sensors, actuators, and energy harvesting," *MRS Bull.* **34**(9), 658–664 (2009).
13. S. Trolrier-McKinstry and P. Muralt, "Thin film piezoelectrics for MEMS," *J. Electroceram.* **12**(1), 7–17 (2004).
14. J. F. Shepard, Jr., P. J. Moses, and S. Trolrier-McKinstry, "The wafer flexure technique for the determination of the transverse piezoelectric coefficient (d_{31}) of PZT thin films," *Sens. Actuators A Phys.* **71**(1-2), 133–138 (1998).
15. N. Izyumskaya, Y.-I. Alivov, S.-J. Cho, H. Morkoc, H. Lee, and Y.-S. Kang, "Processing, structure, properties, and applications of PZT thin films," *Crit. Rev. Solid State Mater. Sci.* **32**(3-4), 111–202 (2007).
16. V. Stancu, M. Lisca, I. Boerasu, L. Pintilie, and M. Kosec, "Effects of porosity on ferroelectric properties of $\text{Pb}(\text{Zr}_{0.2}\text{Ti}_{0.8})\text{O}_3$ films," *Thin Solid Films* **515**(16), 6557–6561 (2007).
17. P. B. Reid, T. L. Aldcroft, R. Allured, V. Cotroneo, R. L. Johnson-Wilke, V. Marquez, S. McMuldloch, S. L. O'Dell, B. D. Ramsey, and D. A. Schwartz, "Development status of adjustable grazing incidence optics for 0.5 arcsecond X-ray imaging", NASA Tech. Rep. 20140016821, M15–4150, (2014).
18. M.-J. Yim and K.-W. Paik, "Design and understanding of anisotropic conductive films (ACFs) for LCD packaging," in *Proc. IEEE Polymer Electronics Packaging* (IEEE, 1997), paper 5920142.
19. S.-M. Chang, J.-H. Jou, A. Hsieh, T.-H. Chen, C.-Y. Chang, Y.-H. Wang, and C.-M. Huang, "Characteristic study of anisotropic-conductive film for chip-on-film packaging," *Microelectron. Reliab.* **41**(12), 2001–2009 (2001).
20. S. C. Tan, Y. C. Chan, Y. W. Chiu, and C. W. Tan, "Thermal stability performance of anisotropic conductive film at different bonding temperatures," *Microelectron. Reliab.* **44**(3), 495–503 (2004).
21. R. Allured, E. Hertz, V. Marquez, V. Cotroneo, M. Wallace, B. Salmaso, M. M. Civitani, S. Trolrier-McKinstry, A. A. Vikhlinin, G. Pareschi, and P. B. Reid, "Laboratory demonstration of the piezoelectric figure correction of a cylindrical slumped glass optic," *Proc. SPIE* **9905**, 990554 (2016).
22. G. G. Stoney, "The tension of metallic films deposited by electrolysis", *Proceedings of the Royal Soc. London, Series A*, 172–175 (1909).
23. G. C. A. M. Janssen, M. M. Abdalla, F. van Keulen, B. R. Pujada, and B. van Venrooy, "Celebrating the 100th anniversary of the Stoney equation for film stress: Developments from polycrystalline steel strips to single crystal silicon wafers," *Thin Solid Films* **517**(6), 1858–1867 (2009).
24. G. A. C. M. Spierings, G. J. M. Dormans, W. G. J. Moors, M. J. E. Ulenaers, and P. K. Larsen, "Stress in $\text{Pt/Pb}(\text{Zr,Ti})\text{O}_3/\text{Pt}$ thin-film stacks for integrated ferroelectric capacitors," *J. Appl. Phys.* **78**(3), 1926–1933 (1995).
25. S. S. Sengupta, S. M. Park, D. A. Payne, and L. H. Allen, "Origins and evolution of stress development in sol-gel derived thin layers and multideposited coatings of lead titanate," *J. Appl. Phys.* **83**(4), 2291–2296 (1997).
26. R. J. Ong, D. A. Payne, and N. R. Sottos, "Processing effects for integrated PZT: Residual stress, thickness, and dielectric properties," *J. Am. Ceram. Soc.* **88**(10), 2839–2847 (2005).
27. B. A. Tuttle and R. W. Schwartz, "Solution deposition of ferroelectric thin films," *MRS Bull.* **21**(6), 49–54 (1996).
28. B. A. Tuttle, T. J. Garino, J. A. Voigt, T. J. Headley, D. Dimos, and M. O. Eatough, in *Science and Technology of Electroceramic Thin Films*, edited by O. Auciello and R. Waser (Kluwer Academic Publishers, Dordrecht, The Netherlands, 1995) p. 117.
29. B. Noheda, D. E. Cox, G. Shirane, J. A. Gonzalo, L. E. Cross, and S.-E. Park, "A monoclinic ferroelectric phase in the $\text{Pb}(\text{Zr}_{1-x}\text{Ti}_x)\text{O}_3$ solid solution," *Appl. Phys. Lett.* **74**(14), 2059–2061 (1999).
30. C. B. Yeager and S. Trolrier-McKinstry, "Epitaxial $\text{Pb}(\text{Zr}_x\text{Ti}_{1-x})\text{O}_3$ ($0.30 < x < 0.63$) films on (100)MgO substrates for energy harvesting applications," *J. Appl. Phys.* **112**(074107), 1–7 (2012).
31. G. Fox, S. Trolrier-McKinstry, S. B. Krupanidhi, and L. M. Casas, "Pt/Ti/SiO₂/Si substrates," *J. Mater. Res.* **10**(06), 1508–1515 (1995).
32. H. Windischmann, "An intrinsic stress scaling law for polycrystalline thin films prepared by ion beam sputtering," *J. Appl. Phys.* **62**(5), 1800–1807 (1987).
33. J. A. Thornton, "Influence of apparatus geometry and deposition conditions on the structure and topography of thick sputtered coatings," *J. Vac. Sci. Technol.* **11**(4), 666–670 (1974).

34. J. A. Thornton, "The microstructure of sputter-deposited coatings," *J. Vac. Sci. Technol. A* **4**(6), 3059–3065 (1986).
35. G. Carter, "Peening in ion-assisted thin-film deposition: a generalized model," *J. Phys. D Appl. Phys.* **27**(5), 1046–1055 (1994).
36. H. Gao, L. Zhang, W. D. Nix, C.V. Thompson, and, E. Arzt, "Crack-line grain-boundary diffusion wedges in thin metal films," *Acta Mater.* **47**(10), 2865–2878 (1999).
37. M. D. Thouless, J. Gupta, and J. M. E. Harper, "Stress development and relaxation in copper films during thermal cycling," *J. Mater. Res.* **8**(8), 1845–1852 (1993).
38. A. Etenko, T. McKechnie, A. Shchetkovskiy, and A. Smirnov, "Oxidation-protective iridium and iridium-rhodium coatings produced by electrodeposition from molten salts," *ECS Trans.* **3**(14), 151–157 (2007).
39. D. M. Broadway, J. Weimer, D. Gurgew, T. Lis, B. D. Ramsey, S. L. O'Dell, M. Gubarev, A. Ames, and, R. Bruni, "Achieving zero stress in iridium, chromium, and nickel thin films," *Proc. SPIE* **9510**, 95100E (2015).